Renewable Energy 113 (2017) 43–51

Contents lists available at ScienceDirect

Renewable Energy

journal homepage: www.elsevier.com/locate/renene

Efficient $ZnO_{1-x}S_x$ composites from the $Zn_5(CO_3)_2(OH)_6$ precursor for the H_2 production by photocatalysis

Octavio Aguilar-Martínez [a, *], Agileo Hernández-Gordillo [b], Raúl Pérez-Hernández [c], Próspero Acevedo-Peña [d], Alma Arrieta-Castañeda [a], Ricardo Gómez [a], Francisco Tzompantzi [a, **]

[a] Depto. de Química, Área de Catálisis, Universidad Autónoma Metropolitana – Iztapalapa, Av. San Rafael Atlixco No. 189, Iztapalapa, Cd. México 09340, Mexico
[b] Instituto de Investigaciones en Materiales, Universidad Nacional Autónoma de México, Circuito Exterior SN, Ciudad Universitaria, Coyoacán, Cd. México 04510, Mexico
[c] Instituto Nacional de Investigaciones Nucleares, Carretera México-Toluca S/N, La Marquesa, Ocoyoacac, Edo. México 52750, Mexico
[d] CONACyT-Centro de Investigación en Ciencia Aplicada y Tecnología Avanzada, Unidad Legaria, IPN, Cd. México 11500, Mexico

ARTICLE INFO

Article history:
Received 15 February 2017
Received in revised form
26 April 2017
Accepted 14 May 2017
Available online 16 May 2017

Keywords:
H_2 production
$ZnO_{1-x}S_x$ composite
Hydrozincite
Solvothermal

ABSTRACT

$ZnO_{1-x}S_x$ (x = 0.2, 0.5, 0.7, and 1.0) composites were prepared from the *hydrozincite* precursor ($Zn_5(CO_3)_2(OH)_6$) as Zn source by sulfidation during the solvothermal treatment using thiourea as sulfur source at different molar ratio. The sulfurized composites were characterized by XRD, FTIR, TGA, SEM-EDS, N_2 physisorption, UV–vis diffuse reflectance spectroscopy, and photoluminescence. Additionally, photocatalysts were deposited onto ITO coated supports to perform their photoelectrochemical characterization. The sulfurized samples were composed of cubic-ZnO and cubic-ZnS with proportions close to the theoretical ones, given a $ZnO_{1-x}S_x$ heterostructures. Mesoporous composites with large specific surface area (up to 207 $m^2\ g^{-1}$) were obtained. All the obtained composites were evaluated in the production of H_2 from a MetOH-water solution and UV light. The photocatalytic stability of the best composite was also evaluated for five reaction cycles. The photocatalytic properties of the $ZnO_{1-x}S_x$ composite is explained as a function of the generation capacity of electron-hole pairs when the photocatalyst is illuminated jointly with the charge transfer resistance of photocatalysts in a methanol-water solution.

1. Introduction

Oil and coal have been used for a long time as the main sources for producing energy forms such as electrical, mechanical, thermal, etc. The burning of these non-renewable resources generates emissions of polluting gases such as CO_2, CO, NO_x, SO_x, etc., which are harmful to human health in addition to propitiate the global warming [1]. One alternative to obtain clean and renewable energy is the dissociation of water to generate H_2 by means of a photocatalysis process with solar light, using a semiconductor material as photocatalyst. This method simulate the photosynthesis, thus it can be considered as an artificial photosynthesis process [2]. In 1972 Fujishima and Honda [3] reported for the first time the dissociation of water using light on TiO_2 as photocatalyst. In the subsequent years (1982) Yanagida [4] and Reber [5] reported the hydrogen production using ZnS semiconductor using UV light.

Zinc sulfide (ZnS) has two crystal structures: cubic zinc blende (sphalerite) and hexagonal (wurtzite) with large band gap energies of 3.72 and 3.77 eV, respectively [6], and it has been widely studied due to its applications such as photoluminescence device and light-emitting diodes [6]. Various methods such as microwaves, thermal evaporation, coprecipitation, and hydrothermal or solvothermal [6–8] have been used to synthesize ZnS in a variety of forms such as wires, bars, tubes, strips, and leaf-shaped structures or flowers, where each one has specific chemical and physical properties. In this line we have recently reported the synthesis of ZnS from *hydrozincite* ($Zn_5(CO_3)_2(OH)_6$) precursor by the solvothermal

* Corresponding author.
** Corresponding author.
E-mail addresses: octavio_a@xanum.uam.mx (O. Aguilar-Martínez), agileohg@iim.unam.mx (A. Hernández-Gordillo), raul.perez@inin.gob.mx (R. Pérez-Hernández), prosperoster@gmail.com (P. Acevedo-Peña), almamireya@gmail.com (A. Arrieta-Castañeda), gorm@xanum.uam.mx (R. Gómez), fjtz@xanum.uam.mx (F. Tzompantzi).

http://dx.doi.org/10.1016/j.renene.2017.05.049
0960-1481/

method showed high photocatalytic activity in H_2 production [9].

The ZnS is a photocatalyst that has a good efficiency producing H_2 from water in the presence of sacrificial agents such as MetOH, EtOH, and electrolytic solutions (S^{2-}, SO_3^{2-}) [4,5]; this is possible because the positions of the conduction and valence bands of ZnS are adequately favorable for both reducing and oxidizing the water molecule [10]. The use of a sacrificial agent helps to catch the holes generated during the reaction process, thereby decreasing the recombination rate of the photogenerated e^--h^+ pair. However, in some cases, ZnS tends to degrade during the photocatalytic reaction [11,12], reducing their efficiency for H_2 production. Some relevant strategies have been employed to maintain or improve the photocatalytic activity of ZnS for H_2 production, as the doping with cobalt, cerium ions and nitrogen [11,13,14] or by the formation of composite materials such as ZnS-ZnO [15,16].

Although the ZnS is active even without a cocatalyst, the forming of composite materials like heterojunction, formed between two semiconductor materials, significantly improves the photocatalytic properties [17]. The ZnS-ZnO composite has shown to have better photocatalytic properties not only removing organic compounds [18,19], but also for H_2 production under UV light [19,20] or visible light [16,21].

Most of the physical and chemical properties of composite-photocatalytic materials are mainly influenced by the synthesis method and their precursors. Recently, the synthesis of the ZnS-ZnO composite by either ZnO sulfidation or ZnS oxidation with photocatalytic applications has been reported [20,22]. However, the inconvenience of synthesizing this ZnS-ZnO composite is the low specific surface area obtained as a consequence of the thermal treatment used to produce these composites [20,23]. The specific surface area is a very important parameter in a catalyst because the chemical reactions take place on its surface, so the synthesis of composite materials with high specific surface area is of great interest in the design of photocatalytic materials.

As a new strategy to obtain nanostructured ZnO with high porosity (mesoporous material) of different morphologies, it was prepared by annealing the material *hydrozincite* ($Zn_5(CO_3)_2(OH)_6$) [24,25], however, in our knowledge, this *hydrozincite* precursor has never been directly used as a Zn source for the synthesis of $ZnO_{1-x}S_x$ composite.

In the present paper, a simple method for the synthesis of a $ZnO_{1-x}S_x$ mesoporous composite from the gradual sulfidation of the material *hydrozincite* (zinc source) by the solvothermal method in ethanol, varying the amount of thiourea used as a sulfur source, is presented. The composite were characterized by XRD, FTIR, TGA, SEM-EDS, N_2 physisorption, UV–vis diffuse reflectance spectroscopy, and photoluminescence. The mesoporous composite materials were evaluated in the production of H_2 using a MetOH-water solution and the composite with the best photoactivity was identified with the optimal sulfur amount. In order to know the stability of the best photoactive material, it was evaluated during five reaction cycles. Additionally, all mesoporous composites were also characterized by photoelectrochemical using the same MetOH-water solution. The improved photoactivity of the $ZnO_{1-x}S_x$ composite was discussed as function of generation capacity of photogenerated electron-hole pairs when the photocalyst is illuminated jointly with the lower charge transfer resistance to drive the hydrogen evolution reaction at the photocatalyst/methanol-water solution interface.

2. Methodology

2.1. Synthesis of hydrozincite and the $ZnO_{1-x}S_x$ composite

2.1.1. Synthesis of hydrozincite (Hz)

At room temperature, in a glass flask, 0.34 mol of zinc nitrate ($Zn(NO_3)_2{\cdot}6H_2O$, J.T.Baker, 99.6% purity) was dissolved in 600 mL of deionized water; subsequently, urea (NH_2CONH_2, Reasol $\geq$ 99% purity) was added for the precipitation process by carbonate generation (molar ratio Zn:urea = 1:3). Then, the transparent homogeneous solution was heated up to boiling point (92 ± 2 °C) under vigorous stirring and refluxed for 36 h. The solution pH generated during the carbonation of Zn was 7.2. The obtained precipitate was washed several times with hot water (at 90 °C) and dried at 90 °C for 48 h. The obtained dried sample was ground and labeled as ***Hz***.

2.1.2. Synthesis of $ZnO_{1-x}S_x$ composites

$ZnO_{1-x}S_x$ (x = 0.2, 0.5, 0.7, and 1.0) composites were synthesized through the sulfidation of the dried *hydrozincite* precursor using thiourea as sulfur source by the solvothermal method in ethanol solvent. In a glass flask containing 100 mL of ethanol (Sigma-Aldrich, HPL grade), 1.0 g of the as-dried *hydrozincite* precursor was added; subsequently, the appropriate amount of thiourea ($(NH_2)_2CS$, Reasol, 99.0% purity) was added, varying the molar ratio of S^{2-}:Zn^{2+} = X:1, where X = 0.2, 0.5, 0.7, and 1.0 mol. The mixture was sonicated for 3 h, and then, the pH was adjusted to that of an alkaline medium (pH = 11.5) with some ethylenediamine drops and taken to a Parr reactor, heating at 140 °C for 10 h [9]. The obtained composite samples were washed with ethanol-water, dried at 90 °C for 24 h and labeled as **HZS_X**, where X represents the S:Zn molar ratio. Separately, ZnS was synthesized by the same procedure mentioned above using zinc nitrate and thiourea with a molar ratio of S^{2-}:Zn^{2+} = 0.7:1.0 and it was identified as **NZS.**

2.2. Characterization of materials

The as-synthesized materials were characterized by X-ray diffraction (XRD) using a Bruker D2 Phaser diffractometer with Cu-Kα radiation. The XRD patterns were recorded in the 2θ scanning interval ranging from 5 to 80°, using a step of 0.01° and a counting time of 0.6 s per step. The thermogravimetric analysis (TGA) was performed using a STA 1000 simultaneous thermal analyzer at a heating rate of 10 °C/min with air flow of 10 mL/s. The morphological study of the materials was carried out using a JOEL JSM-7600F scanning electron microscope with an operating voltage of 20 kV, equipped with energy-dispersive X-ray spectroscopy (Oxford X-Max) for the elemental analysis of the studied samples. N_2 adsorption-desorption isotherms were obtained employing a Quantachrome Autosorb-3B equipment. Before analysis, the samples were degassed at 130 °C for 24 h. The specific surface area was calculated from the BET method. The UV–vis diffuse reflectance spectra were obtained from a Cary-100 spectrophotometer equipped with an integrating sphere; barium sulfate was used as a reference blank. Infrared spectra were obtained using a FTIR Affinity-1 Shimadzu spectrophotometer equipped with an attenuate total reflectance (ATR) accessory, using 800psi of pressure and analyzed in the interval of 600–4000 cm^{-1}. Photoluminescence spectra were obtained from a Luminescence Spectrometer (Perkin Elmer, LS50B) at room temperature and using an excitation wavelength of 325 nm.

2.3. Photocatalytic evaluation

The photocatalytic evaluation of the materials were carried out in a home-made-batch-glass reactor with cylindrical shape (diameter of 5.5 cm and volume of 270 mL) [26]. A quartz tube was placed inside the reactor with a mercury lamp (Pen-Ray) that emits light with a wavelength of 254 nm with 2.16 W of power and 2.2 $mWcm^{-2}$ of intensity. In each reaction, 100 mg of catalyst and 200 mL of a MetOH-water solution (1:1 vol ratio) were used. Before each reaction, the system was purged with N_2 for 10 min in order to

remove O_2 from the system. Throughout irradiation, the reaction system was kept under magnetic stirring at room temperature. The amount of produced H_2 was determined by using a previously plotted calibration curve and it was quantified every hour by employing a gas chromatograph equipped with a TCD detector, Shin-carbon column and using N_2 as carrier gas.

In addition, the photocatalytic stability test for the best composite was also realized for five reaction cycles. In each reaction cycle the photocatalyst was recovered and new MetOH-water solution was used, and following the same procedure above described.

2.4. (Photo) electrochemical characterization

Electrochemical characterization (open circuit potential "OCP" and electrochemical impedance spectroscopy "EIS") was performed in a conventional three-electrode cell. To prepare photocatalyst films samples, 100 μL of 30 mgmL^{-1} HZS_x suspension in ethanol, was deposited on a clean ITO coated substrates (Aldrich, $R_s = 15–25$ Ωcm^{-2}) of 1.25 × 2.5 cm, which was placed inside a spin coater under a rotation at 1000 rpm during 30 s. The as-prepared photocatalyst films were dried at 80 °C during 2 h to evaporate as much solvent as possible. Finally, a squared area of 0.5 × 0.5 cm was delimited to perform the photoelectrochemical measurements in a 0.03 M $KClO_4$ 1:1 MetOH-water: electrolyte, using the same apparatus as in previous reports [27].

3. Results and discussion

3.1. X-ray diffraction of hydrozincite and $ZnO_{1-x}S_x$ composites

Zinc hydroxide carbonate ($Zn_5(CO_3)_2(OH)_6$) was synthesized by the precipitation method, where their diffraction peaks (Fig. S1) correspond to well-crystallized-monoclinic *hydrozincite* (JCPDS No. 54-0047) as was previously reported [9]. When *hydrozincite* was sulfurized using a low amount of thiourea (0.2 mol of S^{2-}) by the solvothermal treatment, the obtained **$HZS_{0.2}$** sample exhibited intense diffraction peaks mainly at 2θ equal to 31.75, 33.41, and 36.32°, which correspond to the (100), (002) and (101) planes, respectively, of the cubic-zincite of ZnO (JCPDS No. 36–1452), however, additional small broadening diffraction planes like (111), (220) and (311), located at 2θ equal to 28.65, 47.91 and 56.35°, respectively, are also observed (Fig. 1A), corresponding to cubic-sphalerite of ZnS (JCPDS No. 05–0566). The main diffraction peaks of *hydrozincite* precursor are not observed, indicating that it was almost transformed into ZnO, but partially sulfided to ZnS. As the S^{2-} amount increases from 0.5 to 1.0 mol, the ZnS diffraction planes become most intense while the ZnO diffraction peaks are completely decreased, indicating that the sulfidation of *hydrozincite* was complete. The presence of both ZnS and ZnO crystalline structures indicates the formation of a $ZnO_{1-x}S_x$ composite [19,21]. The broadening diffraction peaks of cubic-sphalerite phase, indicates that ZnS is in nanocrystalline regime.

Fig. 1B shows the diffractograms in the region of the most intense peaks with their corresponding deconvolution for the **HZS_x** composite. As for the **$HZS_{0.7}$** composite, low intensity peaks can be observed (blue circles in Fig. 1B), which appears to be overlapped by the broadening peaks of cubic-sphalerite phase. This indicates the presence of a low ZnO amount in ZnS matrix. The average crystal size was determined in the direction perpendicular to the plane (111) of ZnS (sphalerite) and (101) of ZnO (zincite) by Scherrer equation [28]. Table 1 shows the average crystal size of ZnS and ZnO in the $ZnO_{1-x}S_x$ composites. The crystal size of ZnS in all **HZS_X** composites is < 4 nm, which is less than the limited XRD detection [29]. For **$HZS_{0.5}$** and **$HZS_{0.2}$** samples, the crystal size of ZnO is ~12 and ~9 nm, respectively. These results indicate that the *hydrozincite* precursor can be sulfided to ZnS (sphalerite), obtaining a crystal size in the order of a few nanometers, and the proportion ZnO in the $ZnO_{1-x}S_x$ composites strongly depends of the used S^{2-} amount.

With the main to compare the influence of the zinc source in the formation of $ZnO_{1-x}S_x$ composite (0.7 mol of S^{2-}), zinc nitrate precursor was used. The XRD patterns and their corresponding deconvolution in the region of the most intense peaks for the **NZS** material (Fig. S2), showed that this sample presented diffraction planes of cubic-sphalerite (JCPDS No. 05–0566) and the hexagonal-wurtzite phase (JCPDS No. 36–1450), however, despite the used molar ratio of S^{2-}:Zn^{2+} = 0.7:1.0, diffraction peaks of the ZnO could be expected, but they were absent, indicating that ZnO was hardly formed. This fact was verified in a synthesis process using a zinc nitrate precursor without adding thiourea by the same procedure mentioned above, where the ZnO formation was completely negligible.

From this result, it can be seen that in the ZnS, sulfided from the *hydrozincite* precursor sample, sphalerite is the predominant phase and the heterostructured $ZnO_{1-x}S_x$ composites can be modulated by varying the thiourea amount. In addition, it was possible to control the particle size of the ZnS (sphalerite). On the other hand, when the zinc nitrate precursor is used, the heterostructured $ZnO_{1-x}S_x$ composite is not possible to be obtained.

3.2. Thermogravimetric analysis

The TGA of the *hydrozincite* precursor (Fig. S3) showed a strong weight loss (21.1%) in the range of 150–260 °C due to the decomposition of ***Hz*** to ZnO. Above 260 °C it presented a small weight loss (2.2%) corresponding to the residual elimination. The total weight loss (23.3%) is close to the theoretically calculated value, as was previously reported [9].

When *hydrozincite* is sulfided with different amounts of S^{2-} by solvothermal treatment, $ZnO_{1-x}S_x$ composites are formed. The TGA of the obtained $ZnO_{1-x}S_x$ composites exhibited different thermal processes (Fig. 2). In the temperature interval ranging from 25 to 260 °C, the composites have mass losses between 3.5 wt%, which correspond to the desorption of water and solvent. In the interval ranging from 260 to 505 °C, a gradual mass loss occurred and in the temperature interval from 505 to 610 °C, the highest mass loss corresponding to the total phase transition of ZnS to ZnO [30,31]. In this temperature interval, the ZnS (**HZS)** material featured a total weight loss of 13% that was slightly lower than the calculated theoretical value (16.5 wt%), such behavior also occurred with the rest of the materials. The explanation of this result is that at temperatures below 505 °C there is a partial oxidation of ZnS to ZnO [22,32]. This fact was confirmed by the XRD of the **HZS** material calcined at 500 °C (Fig. S4), where the well-defined diffraction planes of ZnO was observed due to the partial oxidation of ZnS. The order of the mass loss is 2.1, 5.8, 10.9 and 13.1 wt%, which increased with the percent of oxidation of ZnS to ZnO, respectively. This arrangement is due to the different S^{2-} contents present in formed $ZnO_{1-x}S_x$ composites.

3.3. Infrared spectroscopy

Fig. S5 shows the infrared spectra of the all materials and they showed vibrational bands at 3290 and 1639 cm^{-1}, which are assigned to vibration of O–H groups that may be from small quantity of H_2O adsorbed on the sample [9,22]. The adsorption bands in 1566 and 1010 cm^{-1}, corresponding to the stretching vibrations of $-NH_2$, and C-N bonds, respectively, of the ethylenediamine organic, where it is linked to superficial Zn^{2+} ions on the ZnS surface, originated from the $M(EN)^{2+}$ complex [9,22]. The presence

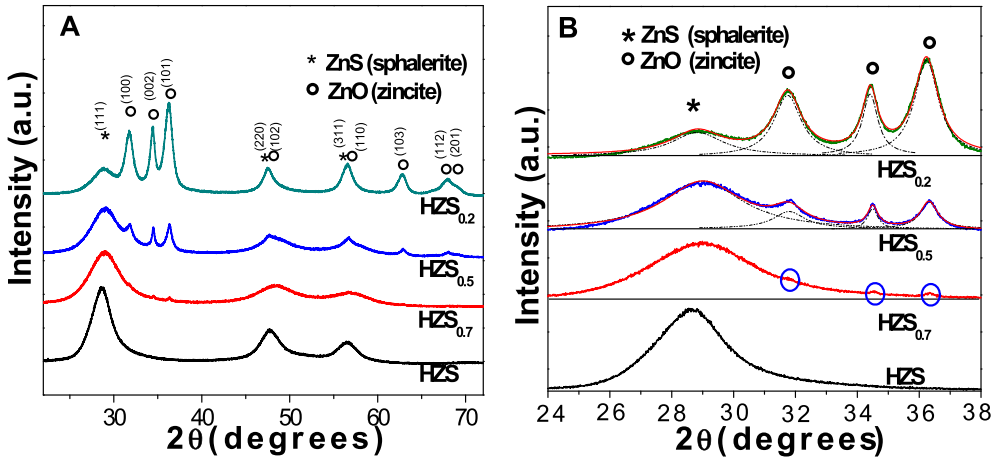

Fig. 1. A) XRD and B) deconvolution of the most intense peaks of XRD of **HZS$_X$** materials.

Table 1
Average crystal size (L), specific surface area (S_{BET}) and band gap energy (Eg) of the synthesized materials.

Material	$L_{(111)}$ ZnS (nm)	$L_{(101)}$ ZnO (nm)	S_{BET} ($m^2\ g^{-1}$)	Eg (eV)
HZS$_{0.2}$	4.1	8.9	108	3.2
HZS$_{0.5}$	<4	12.2	183	3.3
HZS$_{0.7}$	<4	–	207	3.6
HZS	<4	–	160	3.6

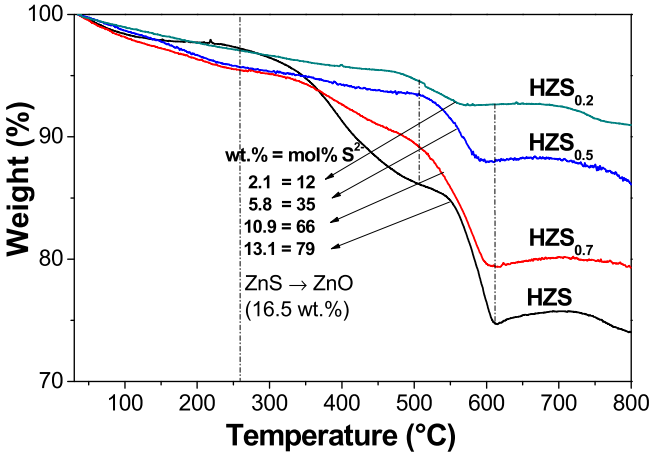

Fig. 2. Thermogravimetric analysis of **HZSx** composite samples.

of this complex is better observed in the **HZS** and **HZS$_{0.7}$** composites. The presence of water and ethylenediamine confirm that they are adsorbed on the composite surface as impurities, as was suggested by thermogravimetric analysis.

3.4. Scanning electron microscopy and energy dispersive spectroscopy

The morphological characteristics of the synthesized $ZnO_{1-x}S_x$ composites were observed by SEM, Fig. 3A–C. The sulfidation percentage of the *hydrozincite* sample affects the morphology of the composites. For the **HZS$_{0.5}$** and **HZS$_{0.7}$** samples, the morphology of the particles is like agglomerates constituted by small particles, but when *hydrozincite* is completely sulfided (**HZS**), flake-shaped particles are obtained. Fig. 3D–F shows the mapping element distribution (Zn, S and O) for the selected **HZS$_{0.7}$** composite. It can be clearly seen that the elements of Zn, S and O are homogeneously distributed throughout the analyzed sample, indicating that the heterostructures of the $ZnO_{1-x}S_x$ composites are well formed, this finding corroborate the results obtained by XRD of this sample.

The elemental analysis (EDS) was performed for the synthesized **HZS$_X$** composite, which is featured in Table 2. The **HZS$_{0.5}$** and **HZS$_{0.7}$** composites and the **HZS** sample showed atomic ratios of S:Zn = 0.50, 0.75, and 0.94, respectively, which are very close to the theoretically calculated values. By contrast, for the **NZS** sample, the atomic ratio of S:Zn is 0.92, close to that obtained with **HZS** sample and to that typically obtained for ZnS (0.99). It is due to that ZnO was hardly formed, confirming that the **NZS** sample is composed only of ZnS. This fact may be due to a shortage of either H_2O or O_2 in the reaction system because they are indispensable for the ZnO formation [33]. This event confirms that the S^{2-} ions added to the system fully react with Zn^{2+} to form the sphalerite and wurtzite ZnS phases. The atomic relation of O:Zn for each of the photocatalysts is greater than the theoretically calculated, this is due to the presence of impurities such as water adsorbed on the material, as was suggested by thermogravimetric analysis (Fig. 2) and FTIR (Fig. S5). For the **NZS** material, despite that ZnO was not detected by XRD, the atomic ratio of O:Zn is slightly higher than that of **HZS$_{0.7}$** sample, which may be due to the water adsorbed on the materials (see Fig. S5).

3.5. Textural properties

Fig. 4 shows the N_2 adsorption-desorption isotherms of the synthesized materials. All the composites showed type IV isotherms corresponding to mesoporous materials. The **NZS** material and the composites prepared with amounts of $S^{2-} \geq 0.5$ mol showed H4-type hysteresis loops that correspond to slit-shaped pores with uniform sizes and shapes [34]. The **HZS$_{0.2}$** composite showed an H3-type hysteresis loop that corresponds to materials such as plates, but with non-uniform sizes [34]. The shape change of the hysteresis loop is probably due to a different content of ZnO in the sulfide composite. The sulfidation of the *hydrozincite* precursor induced the formation of mesoporous $ZnO_{1-x}S_x$ composite materials with high specific surface area. Table 1 shows the specific surface area for each composite material. At low S^{2-} amounts (0.2 mol), the surface area is 108 $m^2\ g^{-1}$, but it is increased up to 207 $m^2\ g^{-1}$ when the S^{2-} amount was increased to 0.7 mol. The high specific surface area of the **HZS$_{0.7}$** composite can be explained by the fact that it consists of agglomerated mesoporous particles (Fig. 3B). The order of the specific surface areas of the **HZS$_X$**

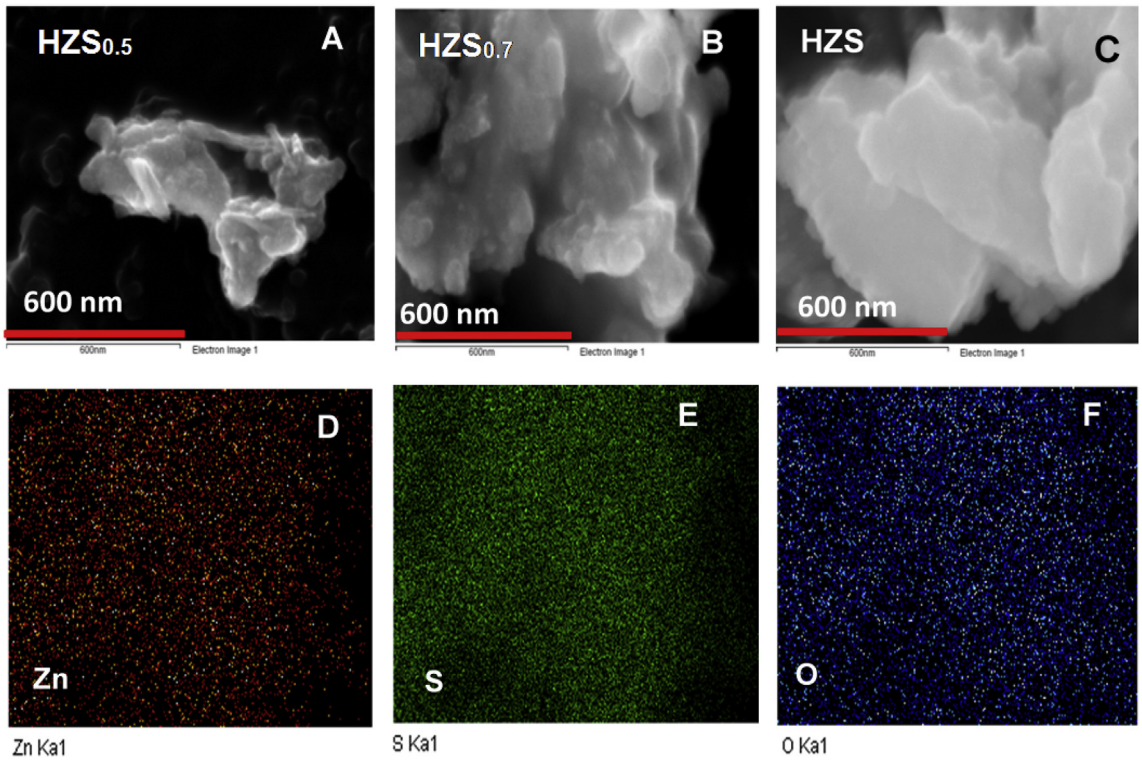

Fig. 3. SEM images of A) **$HZS_{0.5}$**, B) **$HZS_{0.7}$**, C) **HZS** and D)–F) Elemental mapping of Zn, S and O for selected **$HZS_{0.7}$** sample.

Table 2
EDX analysis of the synthesized $ZnO_{1-x}S_x$ composites.

Material	Atomic %			S:Zn atomic ratio	O:Zn atomic ratio
	Zn	S	O		
$HZS_{0.5}$	41.12	20.50	38.38	0.50	0.93
$HZS_{0.7}$	42.68	32.00	25.32	0.75	0.59
HZS	39.53	36.99	23.48	0.94	0.56
NZS	38.75	36.13	25.12	0.92	0.65

composites is **$HZS_{0.7}$ > $HZS_{0.5}$ > HZS > $HZS_{0.2}$**. The specific surface area of **HZS** (160 $m^2\ g^{-1}$) is higher than that of **NZS** material (103 $m^2\ g^{-1}$). Based on these results, it is possible to obtain ZnS and $ZnO_{1-x}S_x$ composites with high specific area by the solvothermal method from the precursor ***Hz***, as source of Zn. The obtained surface areas of the synthesized composites are higher than those reported for ZnS and $ZnO_{1-x}S_x$ (<35 $m^2\ g^{-1}$) [20,35]. Fig. S6 shows the pore distribution of the **HZS_X** composites. The materials showed pore distribution between 3.4 and 3.8 nm, which according to the literature corresponds to mesoporous materials [34].

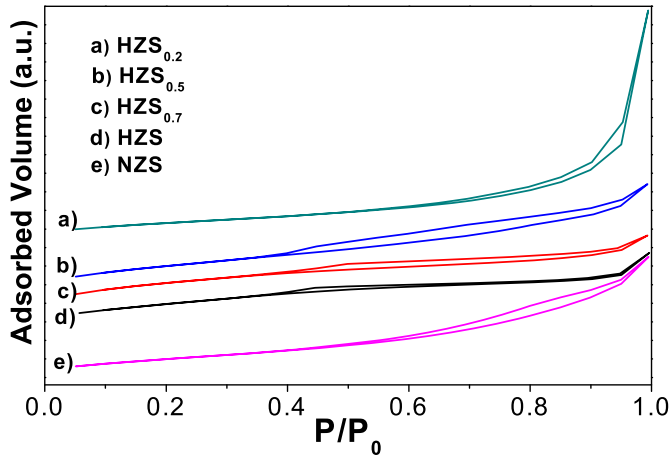

Fig. 4. Adsorption-desorption isotherms of N_2 of the synthesized materials.

3.6. UV–vis diffuse reflectance spectroscopy

Fig. 5A shows the UV–vis diffuse reflectance spectra of the sulfided composites, where an absorption edge between 350 and 405 nm can be seen [36,37]. When the *hydrozincite* precursor is almost completely sulfided, the **$HZS_{0.7}$** and **HZS** samples showed similar absorption edges at about 350 nm due to the electronic transition of the formed ZnS. The wide absorption edge from 350 to 600 nm for the **HZS** sample is probably due to the surface defects caused by ethylenediamine linked to the composite surface [9,38]. By contrast, for the samples partially sulfided with low S^{2-} amounts (0.5 or 0.2 mol), their absorption edges are red-shifted to about 405 nm due to the electronic transition of the formed ZnO, which is more evident in the **$HZS_{0.2}$** sample. For the **$HZS_{0.7}$** sample, a very small absorption edge is observed at 380 nm due to the low ZnO content. This modification regarding the electronic-optical properties suggests the formation of a heterostructure between ZnO and ZnS.

Table 1 shows the band gap energies (Eg) of the sulfided composite, which were obtained from the $(F(R)h\nu)^2$ vs $h\nu$ plot for direct allowed transitions (Fig. 5B) by intersection of the straight line formed by the linear part with the abscissa axis [39]. The band gap energies for the samples with high ZnS contents are close to 3.6 ± 0.1 eV while for the heterostructured **$HZS_{0.5}$** and **$HZS_{0.2}$** materials, containing ZnO, are close to 3.3 ± 0.1 eV.

3.7. Photocatalytic evaluation

Fig. 6A shows the photocatalytic behavior of the sulfided

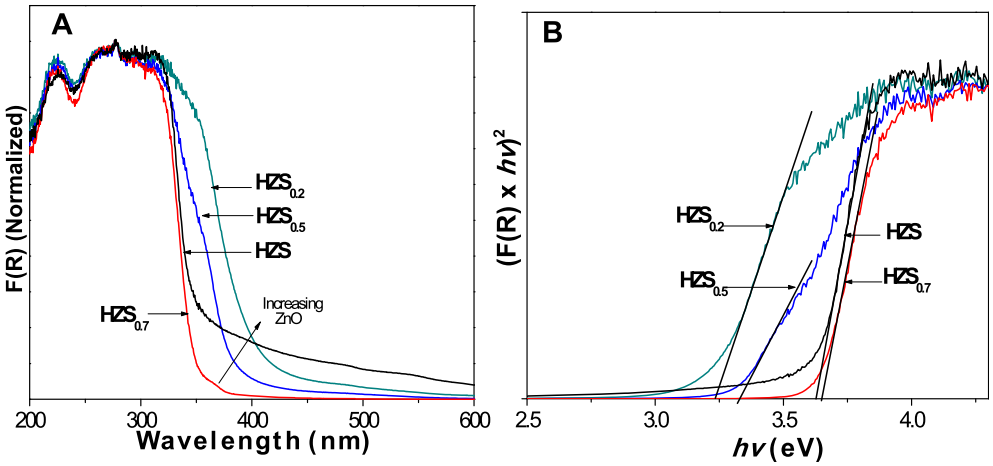

Fig. 5. A) UV–Vis diffuse reflectance spectra and B) graphic of (F(R) x $h\nu$)^2 vs $h\nu$ of the synthesized materials.

composite in the production of H_2. The H_2 amount generated by photolysis was increased as the reaction time progressed, achieving a production rate of 12.6 μmol/h. When the **HZS_X** composite was used, the H_2 amount was drastically increased as the time progressed with a production of H_2 up to 630 μmol in 5 h of reaction, suggesting that the **$HZS_{0.5}$** and **$HZS_{0.7}$** materials are very active for this reaction. The H_2 production rate obtained with all the sulfided composites was standardized (μmol/hg) considering 0.1 g of powdered photocatalyst (Fig. 6B). For the composite $ZnO_{1-x}S_x$ containing low amount of ZnS, its H_2 production rate is very low, but it is increased until 1134.0 μmol/hg when the composite contains the 70% of ZnS. However, when ZnS is fully formed from *hydrozincite*, its photocatalytic activity decreases to 204.6 μmol/hg. The production of H_2 using **NZS** sample was completely negligible (not shown), probably due to the possible high recombination process caused by the presence of two phases (cubic and hexagonal ZnS), causing a negative effect on their photocatalytic properties [9].

These results suggest that there are optimum ZnS and ZnO contents that interact between them to form a heterojunction, improving the photocatalytic activity, which in our case the molar ratio S:Zn is 0.7. Under this condition the electrochemical process induced by the light (water reduction and methanol oxidation) are expected to occur at the highest rate among the materials here synthesized (see photoelectrochemical characterization in section 3.9).

Fig. 7 shows the photocatalytic evaluation of the **$HZS_{0.7}$** material during the five reaction cycles. The photocatalytic activity was maintained during the all reaction cycles, indicating that the material is photochemically stable.

3.8. Photoluminescence (PL)

Fig. 8 shows the photoluminescence spectra of the **HZS_X** materials. All materials showed emission bands between 360 and 600 nm corresponding to the recombination of the photogenerated electron-hole pairs [40,41]. When the material is formed of 20% of ZnS, its intensity of PL is low, but, ZnS contents in the $ZnO_{1-x}S_x$ composite increases, its intensity of PL is also increased, being the material **$HZS_{0.7}$** that showed the highest intensity of PL followed by material **$HZS_{0.5}$**. This fact indicates the formation of structural defects in the composite materials that could act as electron tramps.

3.9. Electrochemical characterization: OCP and EIS

In order to get more insights on the impact of varying the amount of ZnS formed during the solvothermal synthesis of **HZS_X** photocatalysts, over the charge-transfer process under illumination; the

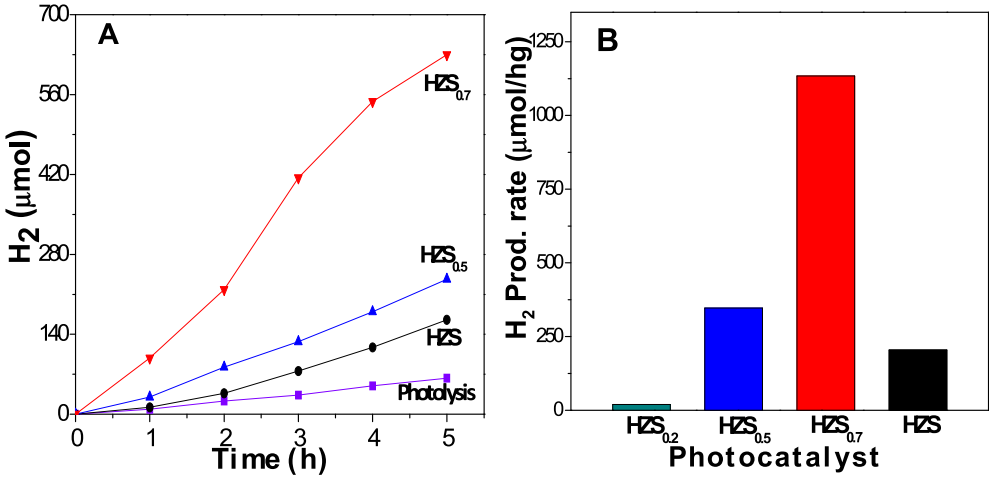

Fig. 6. A) Photocatalytic evaluation of the synthetized materials in the H_2 production from MetOH-water solution, and B) hydrogen production rate per gram of photocatalyst.

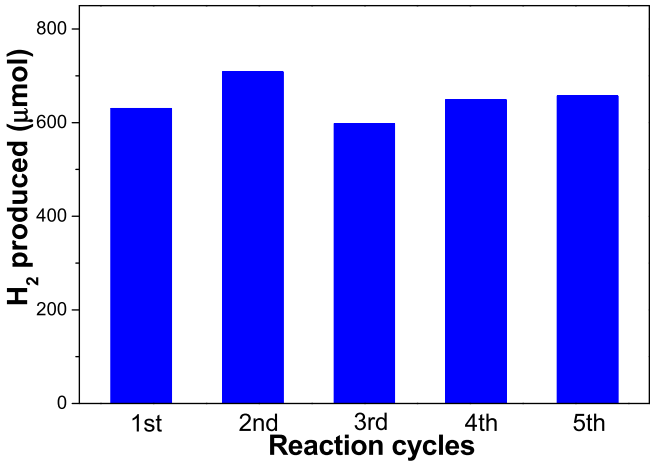

Fig. 7. Five reaction cycles of the **$HZS_{0.7}$** composite.

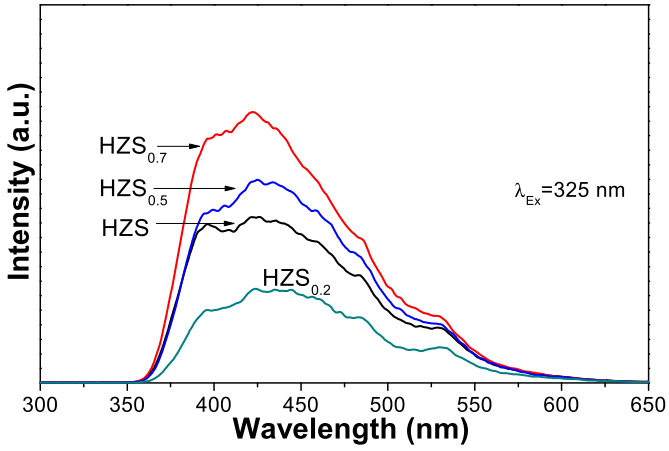

Fig. 8. Photoluminescence spectra of **HZS_X** composites.

photoelectrochemical behavior of photocatalysts supported on ITO coated substrates were characterized in the same solution employed for photocatalytic hydrogen generation test (MetOH-water), but with a supporting electrolyte (0.03 M $KClO_4$). Photoelectrochemical response of photocatalyst is shown in Fig. 9. Photovoltage (difference in the open circuit potential (OCP) under illumination and in dark) is a measurement of the difference between the Fermi level of the electrons in the photocatalyst and the redox potential of species in the electrolyte [42]. The higher the photovoltage generated, more negative is the potential in which electrons are being accumulated under illumination. When photocatalysts films were illuminated, a negative photovoltage was registered, indicating that all films exhibit an n-type behavior, Fig. 9A. However, the largest photovoltage was measured for **$HZS_{0.7}$**, indicating that the more reductive electrons are being photogenerated in this photocatalyst. Furthermore, the photovoltage trend resembles the photocatalytic behavior in Fig. 6, indicating that at more negative potential of the photogenerated electrons, a larger propelling energy is available to perform the hydrogen evolution reaction. The small photovoltage measured for **$HZS_{0.2}$** can be related to the fact that electrons are being accumulated in the ZnO conduction band, which is considerably less negative (electrochemical scale), than conduction band for ZnS [10]. This observation match well with lower photoluminescence observed in Fig. 8, probably due to the electron quenching provoked by the high ZnO contents.

Electrochemical impedance spectra (EIS) of the films were measured at open circuit potential in the dark and under illumination, Fig. 9B. All films exhibited a behavior similar of a dielectric material when tested in the dark. In this case, no electrochemical reactions are taking place over the photocatalysts. However, smaller impedances were registered when films were illuminated, and an arc was formed indicating that light propitiated the charge transfer process through the photocatalyst/electrolyte interface. The lowest impedances were registered for the **$HZS_{0.7}$**, showing that electrochemical reactions (methanol oxidation and water reduction) are taking place at a higher rate than in the other photocatalysts. This behavior agrees the higher hydrogen production rate measured for the semiconductor, and proves that forming a heterojunction between ZnO and ZnS, with optimal ZnS content of 0.7, is a suitable strategy to improve the photocatalytic performance of **HZS** materials obtained from solvothermal synthesis.

3.10. *H_2 production mechanism in the $ZnO_{1-x}S_x$ composite*

The obtained results reveal that an adequate amount of ZnO and ZnS in $ZnO_{1-x}S_x$ composite shows a maximum efficiency in the H_2 production rate. Fig. 10 shows the schematic representation of the positions of the valence and conduction bands of ZnO [43] and of ZnS and $ZnO_{1-x}S_x$ composite (in particular the **$HZS_{0.5}$** and **$HZS_{0.7}$** samples). The positions of valence and conduction bands of **HZS**

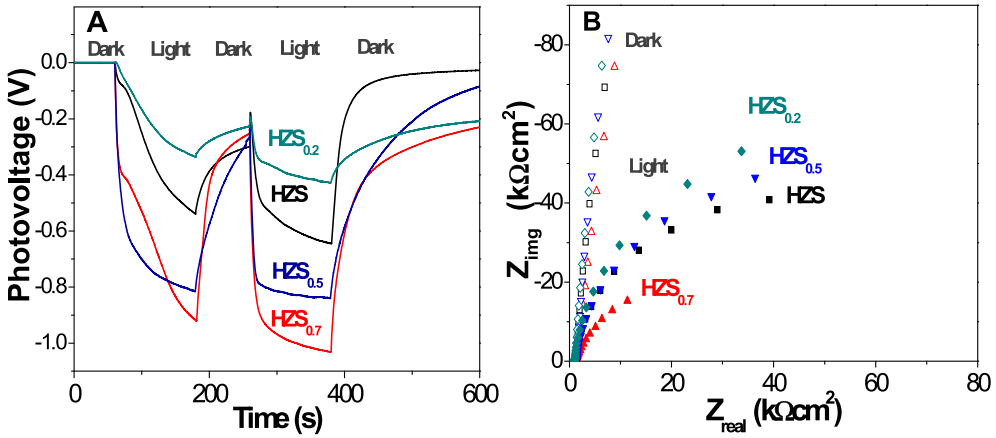

Fig. 9. Photoelectrochemical characterization of synthesized **HZS_X** photocatalysts (indicated in the figure) supported on ITO in a 0.03 M $KClO_4$ 1:1 water: methanol electrolyte: (A) Photovoltage generation (OCP dark − OCP light), and (B) EIS behavior at open circuit potential, measured in the dark (empty symbols) and under illumination (filled symbols).

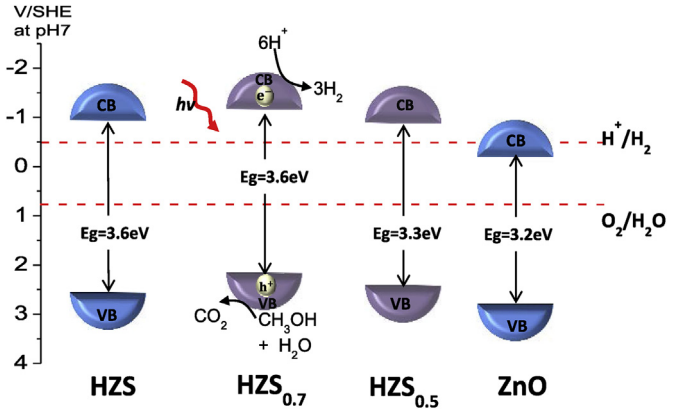

Fig. 10. Representation of the positions of conduction and valence band of ZnO, **HZS**, **$HZS_{0.5}$** and **$HZS_{0.7}$** (at neutral pH), and process of photocatalytic production of hydrogen using methanol as sacrificial agent.

(ZnS), **$HZS_{0.7}$** and **$HZS_{0.5}$** samples were obtained from the value of the flat band potential and these generated from the Mott-Schottky curves at neutral pH conditions, study not shown in this work.

When the formed $ZnO_{1-x}S_x$ composite is irradiated with UV light, the electron-hole pairs are photogenerated. During the lighting process there is an accumulation of electrons and holes in the conduction and valence band, respectively. These are easily transferred from the interface of the photocatalyst to the methanol-water solution to carry out reactions of methanol oxidation and water reduction [44,45]. Photocatalytic activity is improved when the material is forming a heterojunction between ZnO and ZnS, specifically when the molar ratio of S:Zn is 0.7:1, creating structural defects that act as electron tramps.

4. Conclusions

$ZnO_{1-x}S_x$ (x = 0.2, 0.5, 0.7, and 1.0) composites were successfully obtained from *hydrozincite* by sulfidation during the solvothermal method using ethanol as solvent and thiourea as a source of S^{2-} ions. The $ZnO_{1-x}S_x$ heterostructures were composed of cubic-ZnO and cubic-ZnS with proportions close to the theoretical ones. All $ZnO_{1-x}S_x$ composites are mesoporous materials with high surface area (108–207 $m^2\ g^{-1}$). The **$HZS_{0.7}$** composite was the most active photocatalyst with a H_2 production rate of 1134 μmol/hg and it was maintained during the five reaction cycles. The highest photocatalytic activity was attributed to a higher generation of electron-hole pairs when the photocalyst is illuminated jointly with a lower resistance to the transfer of charge from the interface of photocatalyst to the methanol-water solution. These facts are caused from the interaction between ZnS (sphalerite) and ZnO (zincite), forming a heterojunction.

Acknowledgements

Octavio Aguilar would like to thank CONACYT for the scholarship No. 269185. The authors would like to acknowledge the financial support provided by CONACYT (Projects 154994 and *Síntesis de materiales híbridos para la reducción fotocatalítica de hidrógeno* No. CB-2015-01 256410) and CONACYT for the Cátedras-Conacyt/1169 project.

Appendix A. Supplementary data

Supplementary data related to this article can be found at http://dx.doi.org/10.1016/j.renene.2017.05.049.

References

[1] S. Solomon, G.K. Plattner, R. Knutti, P. Friedlingstein, Irreversible climate change due to carbon dioxide emissions, Proc. Natl. Acad. Sci. U. S. A. 106 (2009) 1704–1709.
[2] R. Abe, Recent progress on photocatalytic and photoelectrochemical water splitting under visible light irradiation, J. Photochem. Photobiol. C Photochem. Rev. 11 (2010) 179–209.
[3] A. Fujishima, K. Honda, Electrochemical photolysis of water at a semiconductor electrode, Nature 238 (1972) 37–38.
[4] S. Yanagida, T. Azuma, H. Sakurai, Photocatalytic hydrogen evolution from water using zinc sulfide and sacrificial electron donors, Chem. Lett. 11 (1982) 1069–1070.
[5] J.F. Reber, K. Meier, Photochemical production of hydrogen with zinc sulfide suspensions, J. Phys. Chem. 88 (1984) 5903–5913.
[6] X. Wang, H. Huang, B. Liang, Z. Liu, D. Chen, G. Shen, ZnS nanostructures: synthesis, properties, and applications, Crit. Rev. Solid State Mater. Sci. 38 (2013) 57–90.
[7] G.-J. Lee, S. Anandan, S.J. Masten, J.J. Wu, Photocatalytic hydrogen evolution from water splitting using Cu doped ZnS microspheres under visible light irradiation, Renew. Energy 89 (2016) 18–26.
[8] X. Fang, T. Zhai, U.K. Gautam, L. Li, L. Wu, Y. Bando, D. Golberg, ZnS nanostructures: from synthesis to applications, Prog. Mater Sci. 56 (2011) 175–287.
[9] O. Aguilar, F. Tzompantzi, R. Pérez-Hernández, R. Gómez, A. Hernández-Gordillo, Novel preparation of ZnS from $Zn_5(CO_3)_2(OH)_6$ by the hydro- or solvothermal method for H_2 production, Catal. Today 287 (2017) 91–98.
[10] Y. Xu, M.A.A. Schoonen, The absolute energy positions of conduction and valence bands of selected semiconducting minerals, Am. Mineral. 85 (2000) 543–556.
[11] P. Weide, K. Schulz, S. Kaluza, M. Rohe, R. Beranek, M. Muhler, Controlling the photocorrosion of zinc sulfide nanoparticles in water by doping with chloride and cobalt ions, Langmuir 32 (2016) 12641–12649.
[12] R.M. Navarro Yerga, M.C. Álvarez Galván, F. del Valle, J.A. Villoria de la Mano, J.L.G. Fierro, Water splitting on semiconductor catalysts under visible-light irradiation, ChemSusChem 2 (2009) 471–485.
[13] C.-J. Chang, K.-L. Huang, K.-W. Chu, Y.-H. Wei, I.H. Tseng, Sulfonated graphene oxide-doped zincoxysulfide composites with enhanced photocatalytic hydrogen production performance, Int. J. Hydrogen Energy 41 (2016) 21755–21763.
[14] Y. Zhou, G. Chen, Y. Yu, Y. Feng, Y. Zheng, F. He, Z. Han, An efficient method to enhance the stability of sulphide semiconductor photocatalysts: a case study of N-doped ZnS, PCCP 17 (2015) 1870–1876.
[15] L. Yu, W. Chen, D. Li, J. Wang, Y. Shao, M. He, P. Wang, X. Zheng, Inhibition of photocorrosion and photoactivity enhancement for ZnO via specific hollow ZnO core/ZnS shell structure, Appl. Catal. B Environ. 164 (2015) 453–461.
[16] Y. Li, G. Ma, S. Peng, G. Lu, S. Li, Photocatalytic H_2 evolution over basic zincoxysulfide ($ZnS_{1-x-0.5y}O_x(OH)_y$) under visible light irradiation, Appl. Catal. A General 363 (2009) 180–187.
[17] C. García-Mendoza, S. Oros-Ruiz, A. Hernández-Gordillo, R. López, G. Jácome-Acatitla, H.A. Calderón, R. Gómez, Suitable preparation of Bi_2S_3 nanorods–TiO_2 heterojunction semiconductors with improved photocatalytic hydrogen production from water/methanol decomposition, J. Chem. Technol. Biotechnol. 91 (2016) 2198–2204.
[18] J. Zhao, L. Zhao, X. Wang, Preparation and characterization of ZnO/ZnS hybrid photocatalysts via microwave-hydrothermal method, Front. Environ. Sci. Eng. China 2 (2008) 415–420.
[19] X. Gao, J. Wang, J. Yu, H. Xu, Novel ZnO-ZnS nanowire arrays with heterostructures and enhanced photocatalytic properties, CrystEngComm 17 (2015) 6328–6337.
[20] H.X. Sang, X.T. Wang, C.C. Fan, F. Wang, Enhanced photocatalytic H_2 production from glycerol solution over ZnO/ZnS core/shell nanorods prepared by a low temperature route, Int. J. Hydrogen Energy 37 (2012) 1348–1355.
[21] Z. Wang, S.-W. Cao, S.C.J. Loo, C. Xue, Nanoparticle heterojunctions in ZnS-ZnO hybrid nanowires for visible-light-driven photocatalytic hydrogen generation, CrystEngComm 15 (2013) 5688–5693.
[22] J. Liu, Z. Guo, F. Meng, T. Luo, M. Li, J. Liu, Novel porous single-crystalline ZnO nanosheets fabricated by annealing $ZnS(en)_{0.5}$ (en= ethylenediamine) precursor. Application in a gas sensor for indoor air contaminant detection, Nanotechnology 20 (2009) 125501.
[23] L. Neveux, D. Chiche, D. Bazer-Bachi, L. Favergeon, M. Pijolat, New insight on the ZnO sulfidation reaction: evidences for an outward growth process of the ZnS phase, Chem. Eng. J. 181–182 (2012) 508–515.
[24] N.M.A. Hadia, S. García-Granda, J.R. García, Effect of the temperature on structural and optical properties of zinc oxide nanoparticles, J. Nanosci. Nanotechnol. 14 (2014) 5443–5448.
[25] M. Chen, Y. Wang, L. Song, P. Gunawan, Z. Zhong, X. She, F. Su, Urchin-like ZnO microspheres synthesized by thermal decomposition of hydrozincite as a copper catalyst promoter for the Rochow reaction, RSC Adv. 2 (2012) 4164–4168.
[26] A. Pérez-Larios, R. Lopez, A. Hernández-Gordillo, F. Tzompantzi, R. Gómez, L.M. Torres-Guerra, Improved hydrogen production from water splitting using TiO_2–ZnO mixed oxides photocatalysts, Fuel 100 (2012) 139–143.
[27] Y. Piña-Pérez, F. Tzompantzi-Morales, R. Pérez-Hernández, R. Arroyo-Murillo,

P. Acevedo-Peña, R. Gómez-Romero, Photocatalytic activity of Al_2O_3 improved by the addition of Ce^{3+}/Ce^{4+} synthesized by the sol-gel method. Photodegradation of phenolic compounds using UV light, Fuel 198 (2017) 11–21.
[28] U. Holzwarth, N. Gibson, The Scherrer equation versus the 'Debye-Scherrer equation', Nat. Nano 6 (2011) 534.
[29] V. Uvarov, I. Popov, Metrological characterization of X-ray diffraction methods for determination of crystallite size in nano-scale materials, Mater. Charact. 58 (2007) 883–891.
[30] J.S. Jang, C.-J. Yu, S.H. Choi, S.M. Ji, E.S. Kim, J.S. Lee, Topotactic synthesis of mesoporous ZnS and ZnO nanoplates and their photocatalytic activity, J. Catal. 254 (2008) 144–155.
[31] S.-D. Jiang, Z.-M. Bai, G. Tang, Y. Hu, L. Song, Synthesis of ZnS decorated graphene sheets for reducing fire hazards of epoxy composites, Ind. Eng. Chem. Res. 53 (2014) 6708–6717.
[32] N. Shanmugam, S. Cholan, N. Kannadasan, K. Sathishkumar, G. Viruthagiri, Effect of annealing on the ZnS nanocrystals prepared by chemical precipitation method, J. Nanomater. 2013 (2013) 1–7.
[33] D. Xu, Mechanism of Multidimensional Optical Storage, Multi-dimensional Optical Storage, Springer Singapore, Singapore, 2016, pp. 73–153.
[34] K.S. Sing, Reporting physisorption data for gas/solid systems with special reference to the determination of surface area and porosity (Recommendations 1984), Pure Appl. Chem. 57 (1985) 603–619.
[35] A. Di Paola, M. Addamo, L. Palmisano, Mixed oxide/sulfide systems for photocatalysis, Res. Chem. Intermed. 29 (2003) 467–475.
[36] S.S. Kumar, P. Venkateswarlu, V.R. Rao, G.N. Rao, Synthesis, characterization and optical properties of zinc oxide nanoparticles, Int. Nano Lett. 3 (2013) 30.
[37] S. Biswas, S. Kar, Fabrication of ZnS nanoparticles and nanorods with cubic and hexagonal crystal structures: a simple solvothermal approach, Nanotechnology 19 (2008) 045710.
[38] A. Hernández-Gordillo, F. Tzompantzi, R. Gómez, An efficient ZnS-UV photocatalysts generated in situ from $ZnS(en)_{0.5}$ hybrid during the H_2 production in methanol–water solution, Int. J. Hydrogen Energy 37 (2012) 17002–17008.
[39] R. López, R. Gómez, Band-gap energy estimation from diffuse reflectance measurements on sol–gel and commercial TiO_2: a comparative study, J. Sol-Gel Sci. Technol. 61 (2012) 1–7.
[40] I. Parvaneh, S. Samira, N. Mohsen, Characterization of ZnS nanoparticles synthesized by co-precipitation method, Chin. Phys. B 24 (2015) 046104.
[41] S. López-Romero, M. García-H, Photoluminescence and structural properties of ZnO nanorods growth by assisted-hydrothermal method, World J. Condens. Matter Phys. 3 (2013) 152–157.
[42] D. Guerrero-Araque, P. Acevedo-Peña, D. Ramírez-Ortega, H.A. Calderon, R. Gómez, Charge transfer processes involved in photocatalytic hydrogen production over CuO/ZrO_2–TiO_2 materials, Int. J. Hydrogen Energy 42 (2017) 9744–9753.
[43] C. Kim, S.J. Doh, S.G. Lee, S.J. Lee, H.Y. Kim, Visible-light absorptivity of a zincoxysulfide (ZnO_xS_{1-x}) composite semiconductor and its photocatalytic activities for degradation of organic pollutants under visible-light irradiation, Appl. Catal. A General 330 (2007) 127–133.
[44] X. Chen, S. Shen, L. Guo, S.S. Mao, Semiconductor-based photocatalytic hydrogen generation, Chem. Rev. 110 (2010) 6503–6570.
[45] Y. Lin, R. Lin, F. Yin, X. Xiao, M. Wu, W. Gu, W. Li, Photoelectrochemical studies of H_2 evolution in aqueous methanol solution photocatalysed by Q-ZnS particles, J. Photochem. Photobiol. A Chem. 125 (1999) 135–138.